




Cite this: *Chem. Sci.*, 2023, 14, 8946

All publication charges for this article have been paid for by the Royal Society of Chemistry

## Gram-scale synthesis of MIL-125 nanoparticles and their solution processability†

Kevin Fabrizio,  Eoghan L. Gormley, Audrey M. Davenport, Christopher H. Hendon \* and Carl K. Brozek \*

Although metal–organic framework (MOF) photocatalysts have become ubiquitous, basic aspects of their photoredox mechanisms remain elusive. Nanosizing MOFs enables solution-state techniques to probe size-dependent properties and molecular reactivity, but few MOFs have been prepared as nanoparticles (nanoMOFs) with sufficiently small sizes. Here, we report a rapid reflux-based synthesis of the photoredox-active MOF  $\text{Ti}_8\text{O}_8(\text{OH})_4(\text{terephthalate})_6$  (MIL-125) to achieve diameters below 30 nm in less than 2 hours. Whereas MOFs generally require *ex situ* analysis by solid-state techniques, sub-30 nm diameters ensure colloidal stability for weeks and minimal light scattering, permitting *in situ* analysis by solution-state methods. Optical absorption and photoluminescence spectra of free-standing colloids provide direct evidence that the photoredox chemistry of MIL-125 involves  $\text{Ti}^{3+}$  trapping and charge accumulation onto the Ti-oxo clusters. Solution-state potentiometry collected during the photochemical process also allows simultaneous measurement of MOF Fermi-level energies *in situ*. Finally, by leveraging the solution-processability of these nanoparticles, we demonstrate facile preparation of mixed-matrix membranes with high MOF loadings that retain the reversible photochromism. Taken together, these results demonstrate the feasibility of a rapid nanoMOF synthesis and fabrication of a photoactive membrane, and the fundamental insights they offer into heterogeneous photoredox chemistry.

Received 3rd May 2023  
Accepted 30th July 2023

DOI: 10.1039/d3sc02257a

rsc.li/chemical-science

Tuning photocatalyst performance requires direct and molecular-level insight into the underlying photoredox mechanisms. For example, the optimization of homogeneous photoredox catalysts in recent years relies on knowing the effect of small atomistic changes to catalyst sterics and redox potentials.<sup>1,2</sup> Such structure–function relationships are typically established with a range of solution-state techniques that afford *in situ* insight. Whereas probing molecular aspects of solid-state photocatalysts remains an outstanding challenge, the design of colloidal semiconductor nanocrystals into sophisticated photocatalysts has relied on studying them with solution-state methods, enabled by sub-50 nm sizes that reduce light scatter during spectroscopic measurements.<sup>3</sup> Metal–organic frameworks (MOFs) bridge these two classes by combining vast molecular diversity with the architecture of a solid-state lattice. In the context of catalysis, the well-defined and synthetically tunable nanopores offer a platform for controlling substrate diffusion,<sup>4,5</sup> while the lattice provides matrix stabilization of reactive species otherwise unisolable as small molecules.<sup>6,7</sup> Although MOFs have become widely studied as heterogeneous

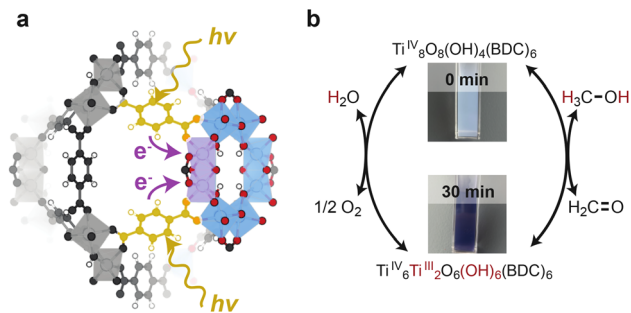
photocatalysts, clear structure–function relationships remain elusive without *in situ* solution-state analysis. Preparing MOFs as nanoparticles smaller than 50 nm would minimize their light scatter and improve colloidal stability during solution-state spectroscopy, electrochemistry, and other *in situ* methods critical to building a molecular understanding of this distinct class of photocatalysts.

Among photoactive MOFs, those containing Ti centers are particularly attractive as molecularly tunable materials because the Ti and surrounding ligand orbitals dominate the frontier orbitals of the MOF. As a result, optical gaps may be controlled by altering the energetics and composition of the Ti ligand sphere.<sup>8–12</sup> For example, modifying  $\text{Ti}_8\text{O}_8(\text{OH})_4(\text{terephthalate})_6$  (MIL-125) to  $\text{Ti}_8\text{O}_8(\text{OH})_4(4\text{-amino-terephthalate})_6$  ( $\text{NH}_2$ -MIL-125) decreases the optical gap from  $\sim 4.0$  eV to 2.6 eV.<sup>13</sup> Light absorption by these materials can be leveraged to achieve photoredox transformations, either by oxidation from photo-generated holes in the HOMO (valence band) or by reduction from photogenerated electrons promoted to the LUMO (conduction band), acting either as photosensitizers for shuttling charges to co-catalysts<sup>14</sup> or as photocatalysts themselves.<sup>15</sup> Dan-Hardi *et al.*<sup>16</sup> demonstrated that MIL-125 irradiated across its optical gap in the presence alcohols induces a photochromic change of the MOF from white to black. Corroborated by EPR measurements,<sup>16</sup> the authors proposed a mechanism shown in

Department of Chemistry and Biochemistry, Material Science Institute, University of Oregon, Eugene, OR 97403, USA. E-mail: cbrozek@uoregon.edu

† Electronic supplementary information (ESI) available. See DOI: <https://doi.org/10.1039/d3sc02257a>





**Scheme 1** (a) Structural representation of the photodoping process in MIL-125. Photoexcited electrons transfer from benzenedicarboxylate to the Ti centers. (b) Chemical representation of the photodoping process in MIL-125 as proposed by Dan-Hardi *et al.*<sup>13</sup> Photoexcitation in the presence of sacrificial reductants (methanol) leads to trapping of  $\text{Ti}^{3+}$  centers balanced by  $\text{H}^+$  by quenching HOMO (linker)-centered holes through methanol oxidation. This reaction manifests qualitatively as a white-to-black color transformation of the MOF.

Scheme 1 involving accumulation of charges in the form of  $\text{Ti}^{3+}$  centers in the Ti-oxo clusters and hole quenching achieved by alcohol oxidation. Since this seminal report, photochemical electronic doping, termed “photodoping”, has been demonstrated for a variety of MOFs containing Ti-oxo clusters,<sup>15,17–19</sup> and mechanistic aspects have been analyzed in terms of proton-coupled electron transfer theory.<sup>20,21</sup> Despite these advancements, direct evidence of  $\text{Ti}^{3+}$  formation remained unobserved and *in situ* measurement of any MOF during photoredox conditions still poses an outstanding challenge.

Here, we report a rapid reflux-based synthesis of MIL-125 nanoparticles to access sizes below 30 nm with indefinite colloidal stability and BET surface areas exceeding that of the bulk, stemming from the higher surface-to-volume ratio in the nanoparticles (Fig. S26–S29†). Afforded by the stability and minimal light scattering of sub-30 nm particles, we employ solution-state spectroscopy to probe the photodoping process *in situ*. These measurements provide definitive evidence of photogenerated  $\text{Ti}^{3+}$  and accumulation of numerous charges at the MOF metal nodes. Electrochemical potentiometry collected during photodoping conditions and voltammetry of free-standing colloids allow determination of the nanoMOF redox potentials underlying this photochemistry. By harnessing the solution processability of the sub-30 nm colloids, MOF–polymer membranes can be fabricated that retain the original photochromic behavior. These results demonstrate the utility of preparing MOFs as nanoparticles for addressing outstanding fundamental questions and progressing MOFs toward industrial implementation.

## Results and discussion

Although nanoMOFs containing Ti-oxo and related Zr-oxo motifs have been previously prepared,<sup>22–24</sup> the smallest reported sizes typically range from 60 to 100 nm. To prepare MIL-125 particles suitable for solution-state techniques (sub-50 nm diameters), we adopted synthetic strategies that would allow

efficient optimization of reaction conditions. Whereas most MOF and nanoMOF synthesis involve solvothermal conditions lasting 8–24 h (ref. 22) that preclude reaction monitoring, reagents were refluxed and products were analyzed as aliquots *ex situ* by PXRD. This approach was inspired by a previous report of using reflux to prepare bulk  $\text{NH}_2\text{-MIL-125}$ , but not nanoparticles.<sup>25</sup> Because nanoMOF syntheses typically rely on organic acids as “crystal growth modulators”,<sup>26</sup> we explored the ability of four monocarboxylic acids to control particle sizes. Previously, we reported a “seesaw model” of MOF growth that relates the ligation strength and acidity of modulators to their ability to generate nanoMOFs of different sizes.<sup>27,28</sup> In this model, modulator serves both as a source of  $\text{H}^+$  and as a ligand that binds to available metal ions. Analysis of the various competing equilibria outlined in the “seesaw” model showed that low concentrations of modulator favor formation of metal–ligand bonds and at high concentration they favor protonation of linker. In other words, the modulator switches from acting as a linker to acting mostly as an acid. This role reversal accounts for the U-shaped size dependence because as a ligand modulator traps small particle sizes, whereas as an acid it keeps linker protonated so that metal ions can diffuse from the bulk to the growing particle surface to furnish larger crystallite sizes. Therefore, we compared “pseudo-linkers” benzoic acid ( $\text{pK}_a = 4.19$ ) and *p*-toluic acid ( $\text{pK}_a = 4.36$ ) versus the small molecular acetic ( $\text{pK}_a = 4.74$ ) and formic ( $\text{pK}_a = 3.75$ ) acids.<sup>29</sup> As a starting point, terephthalic acid and tetrabutyl orthotitanate were refluxed under flowing  $\text{N}_2$  for 6 h in DMF/MeOH with five equivalents of a modulator. Scherrer analysis indicated that under these fixed conditions, benzoic acid yields the smallest nanocrystal sizes (Fig. S3†). The Scherrer analysis was performed by fitting Gaussian band-shapes to each PXRD peak and by using the full-width-half-max and the Scherrer equation to determine the crystallite size (Table S1†). Subsequently, Rietveld refinement was performed to confirm the phase purity of the nanocrystals (Fig. S1†). Although formic acid bears the lowest  $\text{pK}_a$ , benzoic acid generally has comparable or larger metal–ligand stability constants to formic acid, suggesting that once deprotonated it produces smaller nanoparticles by serving as a better competitor with terephthalate. We surmise that the steric similarity between benzoic and terephthalic acids also enhances its mechanistic role. To test the applicability of the “seesaw model” to this system, we explored whether particle sizes would exhibit the predicted U-shaped relationship *versus* modulator equivalents. Therefore, we repeated this synthesis with between 0–10 equivalents of benzoic acid as a modulator. Indeed, this synthetic variation yielded the characteristic U-shaped dependence (Fig. 1a) by both PXRD (Fig. S1†) and SEM (Fig. S9–S13†) sizing, with five equivalents generating the smallest nanocrystals. For quantitative insight into the role of modulator serving as a capping ligand,  $^1\text{H}$  acid digestion NMR spectroscopy was collected on the smallest nanocrystals. Surprisingly, we observed no modulator incorporated as internal defects or surface capping ligands (Fig. S24†), suggesting that modulators function by influencing the competing acid–base and metal–ligand coordination chemistry equilibria, as outlined by the “seesaw model”.



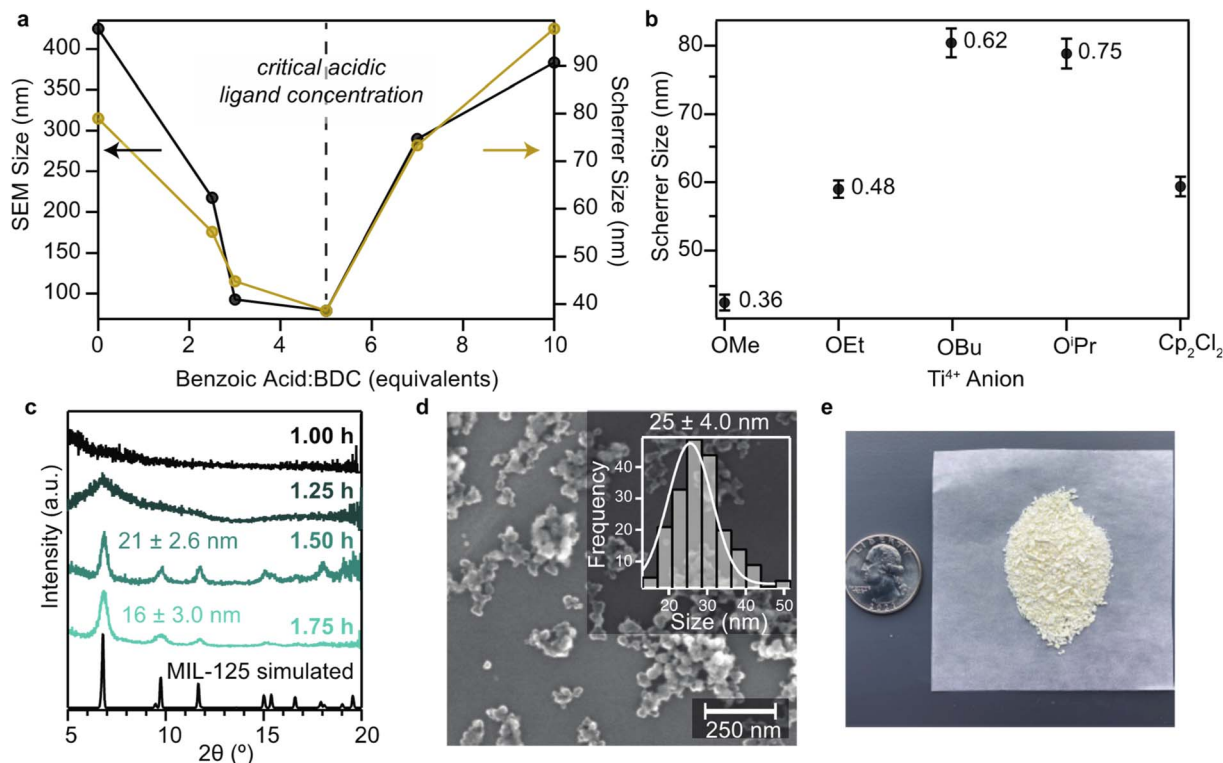


**Fig. 1** (a) MIL-125 nanocrystal sizes versus benzoic acid equivalents under constant reflux conditions (110 °C, 3.33 DMF : 1 MeOH, 1.2 mmol  $Ti(Obu)_4$ ). Sizes reported by both SEM (left) and Scherrer analysis (right). (b) MIL-125 nanocrystal Scherrer sizes versus ligand identity of  $Ti^{4+}$  precursors. Charton steric parameters ( $\nu$ ) for each ligand are included next to each corresponding size. (c) *Ex situ* PXRD patterns and corresponding Scherrer sizes for particles aliquoted during the reaction process. The synthesis involved 5 eq. of BA per BDC and  $Ti(OMe)_4$ . (d) Representative SEM image and particle size for 0.25%  $H_2O$  rel. to DMF. (e) MIL-125 nanoparticle synthesis of a gram shown next to a quarter for scale.

Because the synthesis of Ti-containing MOFs commonly relies on moisture-sensitive  $Ti^{4+}$  alkoxide salts, both the impact of Ti precursor and moisture content were explored as parameters to control particle size. With five equivalents of benzoic acid and by holding constant all other parameters used to study modulator equivalents, as described above, we varied the anion identities of the Ti precursors. To control for moisture exposure, the reactions were carried out in parallel under the same relative humidity. Given that rigorously anaerobic conditions inhibit the formation of MIL-125, we expect that hydrolysis of Ti salts induces the formation of Ti-oxo clusters required for the structural assembly. Performing the standard set of synthetic conditions with titanium(IV) methoxide, titanium(IV) ethoxide, titanium(IV) isopropoxide, titanium(IV) butoxide, or di(cyclopentadienyl)titanium(IV) dichloride produced crystalline MIL-125 nanoparticles of varying sizes, with the methoxide and ethoxide salts consistently producing the smallest nanocrystals (42 and 55 nm by SEM, respectively), as summarized in Fig. 1b. By comparing Charton steric parameters of the alkoxide anions, a direct relationship emerges between Charton parameters and nanocrystal sizes.<sup>30</sup> These results suggest that smaller ligands facilitate the trapping of solubilized  $Ti^{4+}$  and thereby arrest nanoMOF growth. Furthermore, DFT calculations suggest small alkoxide ligands lead to smaller particles sizes because they form strong Ti-OR bonds, thereby decreasing the solubility of

$Ti^{4+}$  and its availability to form MIL-125 (Table S3†). As detailed in our previous report of the “seesaw” model, low metal ion concentrations favor the trapping of small particle sizes.

Given that water content has been shown to control the nanoparticle formation of the Zr-oxo-containing MOF UiO-66,<sup>24</sup> varying quantities of water were added to the MIL-125 reaction mixture prior to reflux. Interestingly, while hydrolysis is necessary (air- and water-free syntheses yielded amorphous products), uncontrolled amounts of water yield  $TiO_2$  byproducts. These results suggest that hydrolysis facilitates the formation of the Ti-oxo clusters. We hypothesized that by controlling the hydrolysis of Ti precursors, free  $Ti^{4+}$  would be liberated slowly to form Ti-oxo clusters prior to ligand assembly. Therefore, aside from small quantities of water (0.25, 0.50, 1.0, and 2.0 vol%), reactions were kept free from ambient humidity under an  $N_2$  atmosphere. Screening these conditions indicated that 0.25% water relative to DMF yielded the smallest nanocrystals of MIL-125 reported at  $25 \pm 4.0$  nm (Fig. 1d). Significantly, the synthesis can also be scaled to produce a gram of uniform crystals (Fig. 1e). This reflux approach with deliberate addition of water applies to other titanium-oxo-cluster MOFs, as well. Fig. S22† shows SEM images of 38 nm  $NH_2$ -MIL-125 nanocrystals prepared by this route, which generates smaller particles with greater colloidal stability and higher yield than previous reports.<sup>22</sup>



Taken together, this search through synthetic parameters implies that using titanium(IV) methoxide, 0.25% H<sub>2</sub>O relative to DMF, and 5 equivalents of benzoic acid yields the smallest nanoparticle sizes. In comparison to the bulk synthesis of MIL-125, which produces particles with a dispersity index ( $\bar{D}$ ) of 0.59, this route creates a narrow size distribution with a  $\bar{D}$  of just 0.17. The  $\bar{D}$  was calculated using the square root of the standard deviation divided by the average particle diameter determined by Scherrer analysis. In addition, the particles remain colloidal stable for at least 6 months, as corroborated by hydrodynamic diameters and dispersity indexes consistent with SEM images and large zeta potentials of *ca.* −30 mV (Table S4†). Additionally, after being dispersed into a colloid, the nanoparticles are recoverable after centrifugation. Furthermore, the reflux-based reaction can be easily scaled to produce gram-scale quantities in a single batch. Lastly, the reaction progress could be monitored to minimize reaction times. By using these conditions as a standard set of reaction parameters, we removed aliquots that were quenched and washed with cold DMF and MeOH and analyzed by PXRD. As shown in Fig. 1c, crystalline MIL-125 nanoparticles form in less than 2 h, whereas typical routes towards bulk and nanoparticle MOFs require half-day or multi-day periods.

The influence of reaction time and temperature were also investigated for the MIL-125 nanoparticle synthesis. Allowing the particles to reflux at 110 °C for 46 h after the start of the synthesis produced small crystals (Fig. S19†). Reflux temperatures of 80 °C and 150 °C were also tested. Performing the synthesis at 80 °C yielded smaller particles in 4 h, whereas the synthesis at 150 °C produced large particles in 1 h (Fig. S20†). We hypothesize that this time dependence indicates MIL-125 nanoparticle sizes are thermodynamically determined by the reaction temperature rather than by extended reaction times.

Given such small particle sizes, and the scalable reaction conditions, we expected improved solution processability to form photoactive MOF-polymer composites at industrially relevant scales. Membranes and films of metal-organic frameworks have long been targeted for water purification, gas separation, liquid-phase separations, electronics, and electrochemical applications,<sup>31,32</sup> but bulk MOF crystals yield inhomogeneous and brittle films incapable of withstanding practically relevant conditions.<sup>33</sup> Thus far, flexible bulk MOF composites (*i.e.*, mixed-matrix membranes, MMMs) have been realized with the inclusion of polymeric binder.<sup>34,35</sup> Despite the potential utility of photoredox-active MMMs, MIL-125 and related MOFs have only been incorporated as bulk crystals and failed to show photochromic activity.<sup>36–38</sup> To demonstrate the improved processability of MIL-125 nanoparticles, we employed an approach originally reported by Cohen *et al.* to create MMM with high (~50 wt%) MOF loadings.<sup>35</sup> Briefly, a polyvinylidene fluoride (PVDF) solution in DMF was mixed with a DMF suspension of the MIL-125 nanocrystals and then the resulting viscous solution was coated onto a glass substrate and allowed to dry in the oven at 70 °C. It should be emphasized that a substrate of any arbitrarily large size could be used given the gram-scale quantities afforded by the reflux route. Finally, the nanoMOF MMM

could be released from the substrate by a short soaking procedure in methanol (Fig. 2a). The MIL-125 nanocrystals remain intact (Fig. 2c) and homogeneously integrated with the polymer binder. Interestingly, while the MOF nanocrystals possess high BET surface areas, the membranes exhibit decreased BET surface areas at 50 m<sup>2</sup> g<sup>−1</sup>. We ascribe this diminishment to polymer entrapment and/or polymer freezing within the large pore matrix of MIL-125. Fig. 2a(IV) shows a small tear within the membrane, highlighting the even distribution of nanoMOF within the PVDF matrix, not just at the surface. To quantitatively measure the MOF content within the polymer, SEM-EDX provided insight into the Ti-to-F concentration. We hypothesized that since titanium should only be found in the MOF, and fluorine in the polymer, that a relative weight percent of titanium should be equal to the amount of MOF loading in the MMM. Experimentally, we synthesized 25 wt% MMM, and by SEM-EDX, the MOF loading was almost identical at 25.85 wt% (Fig. S25 and Table S3†). These results highlight the facile solution-processability of the MOF into a simple, but widely used polymer.

To explore the reactivity and consequent utility of these membranes, we tested whether the MOF retained photoactivity. A 50 wt% MMM was dispersed in a solution of dry benzyl alcohol and placed into an air-free quartz cuvette. Under steady-state UV irradiation, the MOF performed the characteristic white-to-black transformation (Fig. 2b). We posited that although Ti<sup>3+</sup> cannot be seen *via* standard FT-IR techniques, the hole quenching oxidation of an alcohol to an aldehyde could be observed. Accordingly, IR bands consistent with aldehyde carbonyl and alkane stretches became evident in the photodoped thin films, demonstrating that the polymer matrix does not interfere with the MOF photoreactivity. These findings suggest that nano-MIL-125 MMMs may be applied to degrade emerging pollutants, many of which contain alcohol groups (atenolol, bisphenol A, nonyl phenol, *etc.*).

To probe the redox properties of bulk MOFs, decades of research has relied on polymeric binders, such as Nafion, and/or deposition techniques that provide indirect insight into the bare MOFs.<sup>39–42</sup> Recently, our lab demonstrated the first voltammetric analysis of MOF colloids.<sup>43</sup> Here, we harnessed the indefinite stability of MIL-125 nanoparticles to probe their ability to store numerous charges by electrochemical methods. For insight into the energetics of photodoping, the Fermi-level energy of the 25 nm reaction mixture,  $E_F$ , was monitored *in situ* by measuring the open-circuit voltage,  $E_{oc}$ . This approach has been demonstrated to great effect for semiconductor nanocrystals.<sup>44</sup> Fig. 3a plots  $E_{oc}$  over a period of 2.5 h of exposure using a 308 nm, 600 mA LED for a mixture of 25 nm MIL-125 in neat methanol. Upon irradiation,  $E_{oc}$  raises steeply to negative potentials, as expected for photoreduction of Ti. Remarkably, the  $E_{oc}$  stabilized at −0.89 V vs. Fc<sup>+/0</sup>, which is similar to the ~−0.6 mV vs. Fc<sup>+/0</sup> estimated previously for photodoped MIL-125 using optical redox indicators.<sup>45</sup> We note, however, that the technique in the prior report generated huge excess of H<sup>+</sup>, which shifts  $E_F$  to more positive potentials. To investigate whether  $E_F$  under photodoping conditions would be size





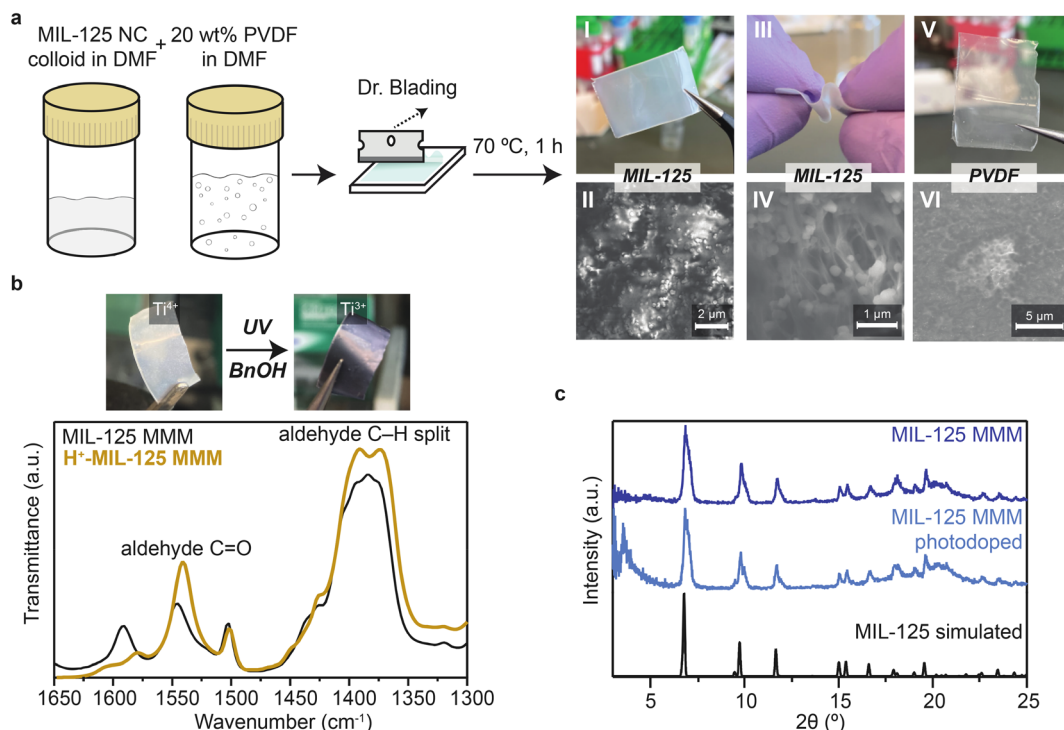


**Fig. 2** (a) Generic reaction scheme for synthesizing MIL-125 MMMs, optical images of a MMM (I and III), top-down SEM images of a MMM, (II and IV), and optical (V) and SEM (VI) images of a standalone polymer membrane. (b) Optical images of a MIL-125 MMM and FT-IR before and after photodoping. (c) PXRD of MIL-125 MMM before and after photodoping highlighting retained crystallinity.

dependent, this measurement was repeated with 87 and 495 nm particles. At steady state under constant illumination, these nanocrystals equilibrated to  $-0.95$  V and  $-0.97$  V vs.  $\text{Fc}^{+/0}$ , respectively, suggesting  $E_F$  reaches more cathodic potentials for larger particles.

With colloidally stable MIL-125 nanoparticles amenable to solution-state spectroscopy due to their sub-30 nm sizes, we sought *in situ* evidence of  $\text{Ti}^{3+}$  formation during photodoping conditions. A  $25 \mu\text{g mL}^{-1}$  mixture of 25 nm MIL-125 particles in methanol was monitored by optical absorption spectroscopy following increments of UV irradiation. Fig. 3c shows the initial spectrum (blue) and subsequent spectra. Immediately after initial light exposure, the first excitonic absorption feature at 4.1 eV begins to bleach. Interestingly, after irradiating for 270 s, the initial excitonic bands give rise to distinct spectral features. The clear isosbestic point seen  $\sim 4.5$  eV, between the blue and yellow traces, suggests the disappearance of an electronic state and the rise of another, highlighted in yellow. With additional irradiation, this state also decayed, giving rise to a final electronic state at 5.5 eV. Photodoping was considered complete at 60 min when spectra ceased changing and this 5.5 eV feature saturated. To highlight this spectral evolution, Fig. 3c includes differential absorption spectra. The final trace in black indicates that overall photodoping bleaches the features centered between 4.0–4.5 eV and generates a new transition at 5.5 eV. These data strongly resemble the spectra evolution of ZnO, CdSe, PbSe, ITO, AZO, and other semiconductor nanocrystals

during photodoping conditions.<sup>44,46–50</sup> In these materials, band-edge bleaching and the concomitant rise of higher-energy bands arise from the blocking of band-gap absorption due to charge accumulation in the conduction band, which also turns on excitation from the valence band into higher-energy unfilled orbitals. Hence, we propose a similar scenario, as illustrated in Fig. 3b. We assign the bleaching of the blue spectrum to blocking of the HOMO–LUMO gap, whereas the yellow and red spectra originate from the promotion of HOMO electrons to higher-lying unoccupied orbitals. To understand the nature of these states arising from photodoping, partial density-of-states diagrams were computed for MIL-125 with varying quantities of  $\text{H}^+-\text{e}^-$  pairs. Fig. 3d shows a systematic increase in the electronic gap between the original HOMO and the new LUMO with charge accumulation. Based on a previous report that electronic states of MIL-125 can be gleaned through Gaussian analysis or by selecting peak maxima from absorption spectra,<sup>51</sup> these computational results suggest the spectrum highlighted in yellow in Fig. 3c corresponds to a photodoped state with roughly four  $\text{H}^+-\text{e}^-$  pairs accumulated on each MIL-125 titanium oxo cluster and that further accumulation occurs until reaching the final state shown in the red spectrum. These results contrast with previous reports suggesting a maximum charge accumulation of between two and ten electrons per MIL-125 cluster.<sup>20,21</sup>

To observe the formation of  $\text{Ti}^{3+}$  as evidenced by the weakly absorbing d–d transitions, these experiments were



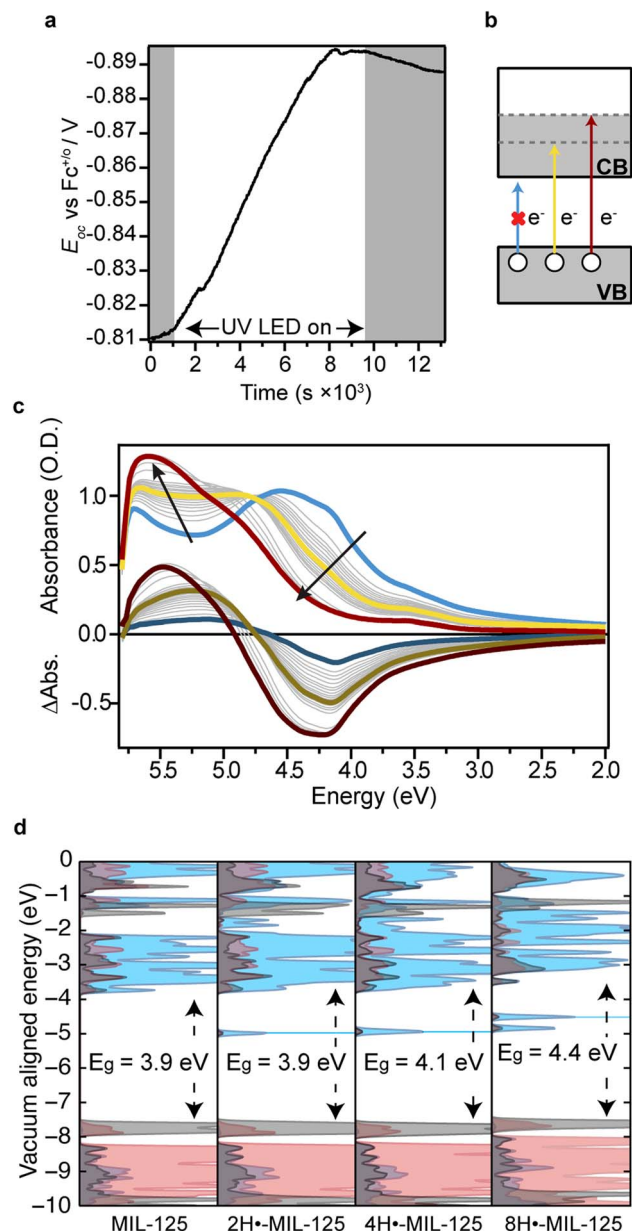


**Fig. 3** (a) *In situ* open-circuit voltage measurements collected during the photodoping process for 150 nm MIL-125 NCs in a 3 mL DMF solution of 0.1 M TBAPF<sub>6</sub> with 0.5 mL methanol. (b) Schematic representation of MIL-125 optical absorption during photodoping process. (c) Solution-state optical absorption spectra of a 25  $\mu\text{g mL}^{-1}$  solution of 25 nm MIL-125 nanoparticles collected *in situ* during the photodoping process in neat methanol. Differential absorption represents the absorption difference at a time point and the initial spectrum (blue). (d) Partial density-of-states diagrams computed for MIL-125 to varying photodoped extents.

repeated at higher concentrations. Fig. 4a plots the undoped absorption spectrum of 25 nm nanoparticles in neat methanol. Shown in the inset is the solution at ten-fold greater concentration, indicating that UV light induces the formation of two absorption features centered at 610 nm and 495 nm, corresponding to 16 400 and 20 200  $\text{cm}^{-1}$ . These

bands are hallmark features of a  $d^1$  transition-metal ion in a pseudo- $O_h$  ligand field subject to symmetry lowering distortions, as exemplified by  $\text{Ti}(\text{H}_2\text{O})_6^{3+}$  complexes.<sup>52,53</sup> Fig. 4b summarizes this assignment and fits the spectra to Gaussian line shapes. By approximating the Ti geometry as  $C_{4v}$  point group symmetry, due to the presence of five oxo groups and one -OH group, we assign the band centered at 20 200  $\text{cm}^{-1}$  to a  ${}^2B_2 \rightarrow {}^2B_1$  transition and the shoulder at 16 400  $\text{cm}^{-1}$  to a  ${}^2B_2 \rightarrow {}^2A_1$  (Fig. 4b).<sup>54</sup> Interestingly, in molecular Ti-oxo clusters, multiple d-d transitions are not observed upon photodoping.<sup>55</sup> To further harness the solution-processability of these nanoMOFs and provide additional insight into the electronic effects of photodoping, solution-state photoluminescence spectra were collected of colloidal particles before and after photodoping. Fig. 4a includes the photoluminescence spectra of colloidal 25 nm MIL-125. An excitation wavelength was selected near the band edge absorption at 280 nm. In undoped conditions, the emission data display a feature centered at 420 nm. To probe the origin of this luminescence, the particles were excited with sub-gap energies as low as 375 nm. Because the feature persisted, we tentatively assign it to radiative relaxation from mid-gap orbitals (Fig. S25†). Interesting, upon photodoping for 2 hours, the higher energy transition decreases in intensity by 33-fold and blueshifts slightly, suggesting the charges relax from a higher energy orbital due to accumulation of charges in the LUMO, as expected for a photodoped material.

The appearance of d-d transitions characteristic of mononuclear  $\text{Ti}^{3+}$  in photodoped MIL-125 suggests that orbitals localize around an individual Ti center, despite the multinuclearity of the metal node and the possibility of delocalized bonding. This observation highlights the unique position of metal clusters on the continuum from molecular redox chemistry to charge accumulation in extended systems. On one hand, the molecular orbital diagrams of multinuclear clusters and carbon allotropes, such as platinum carbonyl clusters, Chevrel compounds, and  $\text{C}_{60}$ , often possess highly degenerate sets of orbitals well suited for charge accumulation.<sup>56–58</sup> When probed through electrochemical methods, however, the redox states appear at discrete energies differing by >100 mV.<sup>59–61</sup> This apparent discrepancy speaks to the failure of orbital diagrams to account for interelectronic effects, such as repulsion and exchange, and ion pairing. Electrochemical potentials of any faradaic event can be understood as a combination of changes to chemical potential and electrostatic potentials,<sup>62</sup> and the interplay of these factors breaks the degeneracy of otherwise delocalized orbitals in clusters, akin to the formation of polarons. Our calculations of MIL-125 under various photodoping conditions indicates the redox chemistry of behaves in a similar manner. Fig. 5 shows the computed geometries and spin density in MIL-125 when undoped, with an uncompensated  $e^-$  and with a  $\text{H}^+e^-$  pair. A single, uncompensated  $e^-$  delocalizes across the entire cluster (middle panel), but when paired with a  $\text{H}^+$ , the wavefunction collapses around a single Ti site (right panel). Spin densities of subsequent  $\text{H}^+e^-$  loadings would similarly localize and the electrochemical potentials required

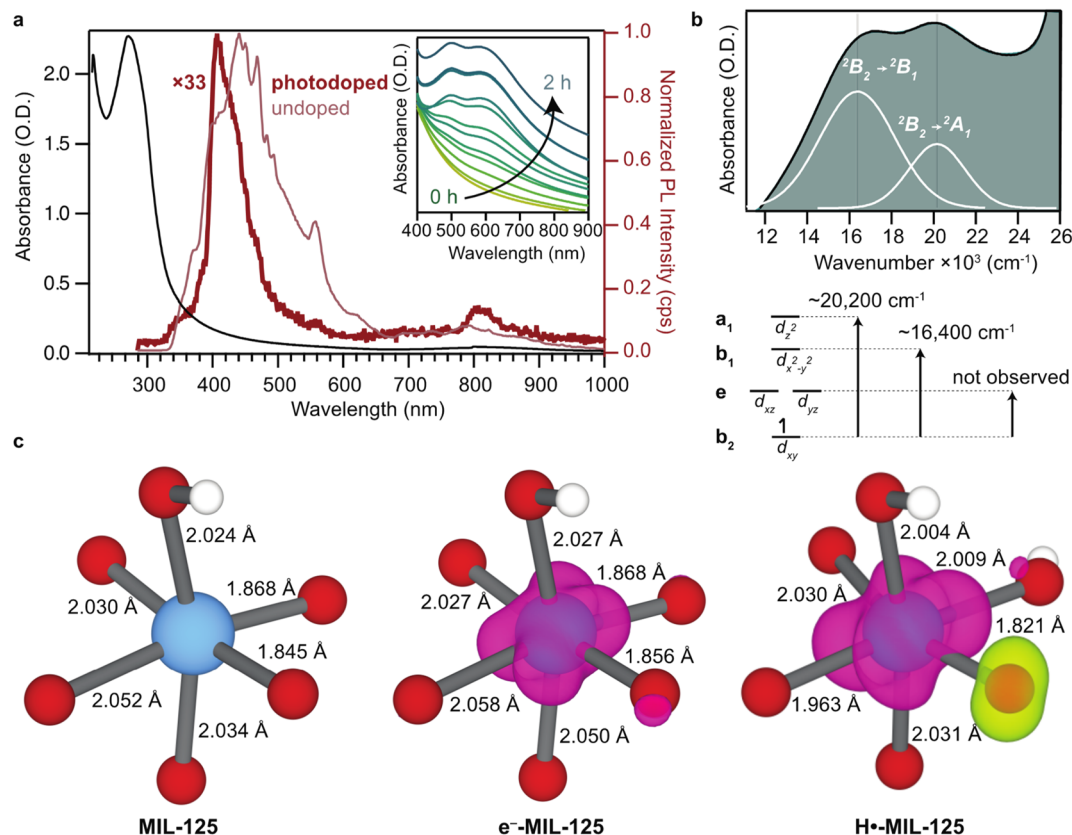


Fig. 4 (a) Solution-state optical absorption and photoluminescence spectra of a 25  $\mu\text{g mL}^{-1}$  colloid of 25 nm MIL-125 nanoparticles. Inset: growth of d-d transitions in a 0.25  $\text{mg mL}^{-1}$  suspension during 2 h photodoping reaction with methanol. (b) Ligand-field analysis of photodoped MIL-125 indicates that two d-d bands arise from Jahn-Teller distorted  $\text{Ti}^{3+}$ . (c) Computed geometries and spin densities of Ti centers in MIL-125 clusters with varying extents of charge accumulation. Pink and yellow denote spin up and spin down density.

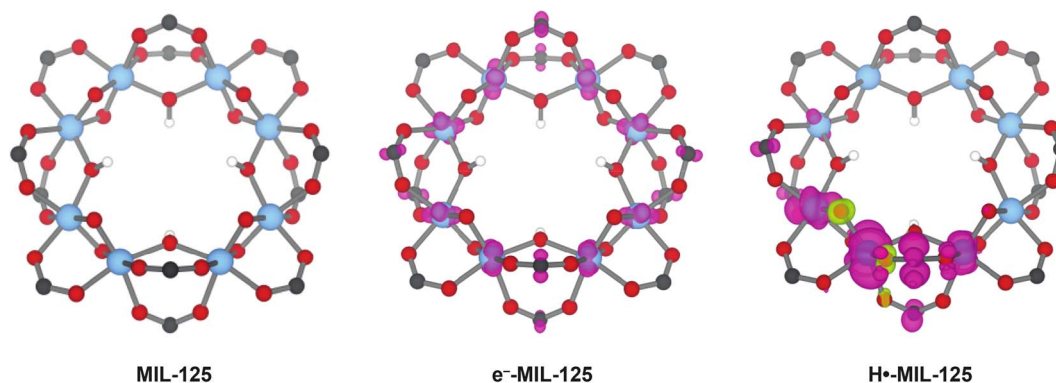


Fig. 5 Computed geometries and spin densities of MIL-125 in varying charge states. Note: only a single cluster from the extended lattice is shown for clarity. Pink and yellow denote spin up and spin down density.

to access these states would depend on the interelectronic, ion-pairing, and atomic rearrangement energies, leading to discrete redox events. Experimental investigations into this behavior are ongoing.

## Conclusion

In summary, we demonstrate a reproducible and rapid synthesis towards sub-30 nm MIL-125 nanoparticles at gram scale with excellent solution-processability as membranes.





The colloidal stability of these nanocrystals enables rare access to solution-state spectroscopy and electrochemistry as tools for probing the heterogeneous photoredox chemistry of MOFs. These insights offer the first direct evidence of  $\text{Ti}^{3+}$  trapping, accumulation of numerous charges per cluster, and the redox potentials associated with these processes.

## Data availability

Data presented in the manuscript is available in machine readable format from <https://doi.org/10.6084/m9.figshare.23826630>.

## Author contributions

K. F., A. M. D. and C. K. B. conceived of the project and co-wrote the manuscript. K. F. carried out the experiments. E. G. and C. H. H. performed computational studies.

## Conflicts of interest

The authors declare no competing interests.

## Acknowledgements

This work made use of the CAMCOR facility of the Lorry I. Lokey Laboratories at the University of Oregon to perform SEM experiments. This material is based upon work supported by the National Science Foundation through the Division of Materials Research under grant no. DMR-2114430 and through the Division of Chemistry under grant no. CHE-2237345. C. H. H. acknowledges the support of the Camille and Henry Dreyfus Foundation. C. K. B. and C. H. H. acknowledge the Research Corporation for Science Advancement (Cottrell Award).

## References

- 1 A. S. Harmata, T. E. Spiller, M. J. Sowden and C. R. J. Stephenson, Photochemical Formal (4 + 2)-Cycloaddition of Imine-Substituted Bicyclo[1.1.1]pentanes and Alkenes, *J. Am. Chem. Soc.*, 2021, **143**, 21223–21228.
- 2 T. Q. Chen, P. S. Pedersen, N. W. Dow, R. Fayad, C. E. Hauke, M. C. Rosko, E. O. Danilov, D. C. Blakemore, A.-M. Dechert-Schmitt, T. Knauber, F. N. Castellano and D. W. C. MacMillan, A Unified Approach to Decarboxylative Halogenation of (Hetero)aryl Carboxylic Acids, *J. Am. Chem. Soc.*, 2022, **144**, 8296–8305.
- 3 Y. Jiang and E. A. Weiss, Colloidal Quantum Dots as Photocatalysts for Triplet Excited State Reactions of Organic Molecules, *J. Am. Chem. Soc.*, 2020, **142**, 15219–15229.
- 4 M. Cai, Q. Loague and A. J. Morris, Design Rules for Efficient Charge Transfer in Metal-Organic Framework Films: The Pore Size Effect, *J. Phys. Chem. Lett.*, 2020, **11**, 702–709.
- 5 A. T. Castner, H. Su, E. Svensson Grape, A. K. Inge, B. A. Johnson, M. S. G. Ahlquist and S. Ott, Microscopic Insights into Cation-Coupled Electron Hopping Transport in a Metal–Organic Framework, *J. Am. Chem. Soc.*, 2022, **144**, 5910–5920.
- 6 C. K. Brozek, J. T. Miller, S. A. Stoian and M. Dinca, NO Disproportionation at a Mononuclear Site-Isolated  $\text{Fe}^{2+}$  Center in  $\text{Fe}^{2+}$ -MOF-5, *J. Am. Chem. Soc.*, 2015, **137**, 7495–7501.
- 7 C. Sun, L. Yang, M. A. Ortuño, A. M. Wright, T. Chen, A. R. Head, N. López and M. Dincă, Spectroscopic Evidence of Hyponitrite Radical Intermediate in NO Disproportionation at a MOF-Supported Mononuclear Copper Site, *Angew. Chem., Int. Ed.*, 2021, **60**, 7845–7850.
- 8 K. Fabrizio, K. A. Lazarou, L. I. Payne, L. P. Twhight, S. Golledge, C. H. Hendon and C. K. Brozek, Tunable Band Gaps in MUV-10(M): A Family of Photoredox-Active MOFs with Earth-Abundant Open Metal Sites, *J. Am. Chem. Soc.*, 2021, **143**, 12609–12621.
- 9 C. H. Hendon, D. Tiana, M. Fontecave, C. Sanchez, L. D'arras, C. Sassoye, L. Rozes, C. Mellot-Draznieks and A. Walsh, Engineering the Optical Response of the Titanium-MIL-125 Metal–Organic Framework through Ligand Functionalization, *J. Am. Chem. Soc.*, 2013, **135**, 10942–10945.
- 10 Y. Fu, D. Sun, Y. Chen, R. Huang, Z. Ding, X. Fu and Z. Li, An Amine-Functionalized Titanium Metal–Organic Framework Photocatalyst with Visible-Light-Induced Activity for  $\text{CO}_2$  Reduction, *Angew. Chem., Int. Ed.*, 2012, **51**, 3364–3367.
- 11 M. W. Logan, S. Ayad, J. D. Adamson, T. Dilbeck, K. Hanson and F. J. Uribe-Romo, Systematic variation of the optical bandgap in titanium based isorecticular metal–organic frameworks for photocatalytic reduction of  $\text{CO}_2$  under blue light, *J. Mater. Chem. A*, 2017, **5**, 11854–11863.
- 12 M. A. Nasalevich, M. G. Goesten, T. J. Savenije, F. Kapteijn and J. Gascon, Enhancing optical absorption of metal–organic frameworks for improved visible light photocatalysis, *Chem. Commun.*, 2013, **49**, 10575–10577.
- 13 Y. Horiuchi, T. Toyao, M. Saito, K. Mochizuki, M. Iwata, H. Higashimura, M. Anpo and M. Matsuoka, Visible-light-promoted photocatalytic hydrogen production by using an amino-functionalized  $\text{Ti(IV)}$  metal–organic framework, *J. Phys. Chem. C*, 2012, **116**, 20848–20853.
- 14 P. Ji, Y. Song, T. Drake, S. S. Veroneau, Z. Lin, X. Pan and W. Lin, Titanium(III)-Oxo Clusters in a Metal–Organic Framework Support Single-Site  $\text{Co(II)}$ -Hydride Catalysts for Arene Hydrogenation, *J. Am. Chem. Soc.*, 2018, **140**, 433–440.
- 15 J. Castells-Gil, N. M. Padial, N. Almora-Barrios, J. Albero, A. R. Ruiz-Salvador, J. González-Platas, H. García and C. Martí-Gastaldo, Chemical Engineering of Photoactivity in Heterometallic Titanium–Organic Frameworks by Metal Doping, *Angew. Chem., Int. Ed.*, 2018, **57**, 8453–8457.
- 16 M. Dan-Hardi, C. Serre, T. Frot, L. Rozes, G. Maurin, C. Sanchez and G. Férey, A new photoactive crystalline highly porous titanium(IV) dicarboxylate, *J. Am. Chem. Soc.*, 2009, **131**, 10857–10859.
- 17 J. Castells-Gil, N. M. Padial, N. Almora-Barrios, R. Gil-San-Millán, M. Romero-Ángel, V. Torres, I. da Silva, B. C. J. Vieira, J. C. Waerenborgh, J. Jagiello, J. A. R. Navarro, S. Tatay and C. Martí-Gastaldo,





- Heterometallic Titanium-Organic Frameworks as Dual-Metal Catalysts for Synergistic Non-buffered Hydrolysis of Nerve Agent Simulants, *Chem*, 2020, **6**, 3118–3131.
- 18 N. M. Padial, J. Castells-Gil, N. Almora-Barrios, M. Romero-Angel, I. da Silva, M. Barawi, A. García-Sánchez, V. A. de la Peña O'Shea and C. Martí-Gastaldo, Hydroxamate Titanium-Organic Frameworks and the Effect of Siderophore-Type Linkers over Their Photocatalytic Activity, *J. Am. Chem. Soc.*, 2019, **141**, 13124–13133.
  - 19 J. Castells-Gil, N. M. Padial, N. Almora-Barrios, I. da Silva, D. Mateo, J. Albero, H. García and C. Martí-Gastaldo, De novo synthesis of mesoporous photoactive titanium(IV)-organic frameworks with MIL-100 topology, *Chem. Sci.*, 2019, **10**, 4313–4321.
  - 20 C. T. Saouma, S. Richard, S. Smolders, M. F. Delley, R. Ameloot, F. Vermoortele, D. E. De Vos and J. M. Mayer, Bulk-to-Surface Proton-Coupled Electron Transfer Reactivity of the Metal-Organic Framework MIL-125, *J. Am. Chem. Soc.*, 2018, **140**, 16184–16189.
  - 21 C. T. Saouma, C.-C. Tsou, S. Richard, R. Ameloot, F. Vermoortele, S. Smolders, B. Bueken, A. G. DiPasquale, W. Kaminsky, C. N. Valdez, D. E. D. Vos and J. M. Mayer, Sodium-coupled electron transfer reactivity of metal-organic frameworks containing titanium clusters: the importance of cations in redox chemistry, *Chem. Sci.*, 2019, **10**, 1322–1331.
  - 22 M. Romero-Angel, J. Castells-Gil, V. Rubio-Giménez, R. Ameloot, S. Tatay and C. Martí-Gastaldo, Surfactant-assisted synthesis of titanium nanoMOFs for thin film fabrication, *Chem. Commun.*, 2021, **57**, 9040–9043.
  - 23 S. Hu, M. Liu, X. Guo, K. Li, Y. Han, C. Song and G. Zhang, Effects of monocarboxylic acid additives on synthesizing metal-organic framework NH<sub>2</sub>-MIL-125 with controllable size and morphology, *Cryst. Growth Des.*, 2017, **17**, 6586–6595.
  - 24 G. E. Decker, Z. Stillman, L. Attia, C. A. Fromen and E. D. Bloch, Controlling Size, Defectiveness, and Fluorescence in Nanoparticle UiO-66 through Water and Ligand Modulation, *Chem. Mater.*, 2019, **31**, 4831–4839.
  - 25 M. Sohail, Y.-N. Yun, E. Lee, S. K. Kim, K. Cho, J.-N. Kim, T. W. Kim, J.-H. Moon and H. Kim, Synthesis of Highly Crystalline NH<sub>2</sub>-MIL-125 (Ti) with S-Shaped Water Isotherms for Adsorption Heat Transformation, *Cryst. Growth Des.*, 2017, **17**, 1208–1213.
  - 26 R. S. Forgan, Modulated self-assembly of metal-organic frameworks, *Chem. Sci.*, 2020, **11**, 4546–4562.
  - 27 C. R. Marshall, E. E. Timmel, S. A. Staudhammer and C. K. Brozek, Experimental evidence for a general model of modulated MOF nanoparticle growth, *Chem. Sci.*, 2020, **11**, 11539–11547.
  - 28 C. R. Marshall, S. A. Staudhammer and C. K. Brozek, Size control over metal-organic framework porous nanocrystals, *Chem. Sci.*, 2019, **10**, 9396–9408.
  - 29 S. Hu, M. Liu, X. Guo, K. Li, Y. Han, C. Song and G. Zhang, Effects of Monocarboxylic Acid Additives on Synthesizing Metal-Organic Framework NH<sub>2</sub>-MIL-125 with Controllable Size and Morphology, *Cryst. Growth Des.*, 2017, **17**, 6586–6595.
  - 30 M. Charton, in *Steric Effects in Drug Design*, Springer Berlin Heidelberg, Berlin, Heidelberg, 1983, vol. 114, pp. 57–91.
  - 31 T. Kitao, Y. Zhang, S. Kitagawa, B. Wang and T. Uemura, Hybridization of MOFs and polymers, *Chem. Soc. Rev.*, 2017, **46**, 3108–3133.
  - 32 G. Liu, V. Chernikova, Y. Liu, K. Zhang, Y. Belmabkhout, O. Shekhah, C. Zhang, S. Yi, M. Eddaoudi and W. J. Koros, Mixed matrix formulations with MOF molecular sieving for key energy-intensive separations, *Nat. Mater.*, 2018, **17**, 283–289.
  - 33 W. S. Chi, B. J. Sundell, K. Zhang, D. J. Harrigan, S. C. Hayden and Z. P. Smith, Mixed-Matrix Membranes Formed from Multi-Dimensional Metal-Organic Frameworks for Enhanced Gas Transport and Plasticization Resistance, *ChemSusChem*, 2019, **12**, 2355–2360.
  - 34 A. Knebel, A. Bavykina, S. J. Datta, L. Sundermann, L. Garzon-Tovar, Y. Lebedev, S. Durini, R. Ahmad, S. M. Kozlov, G. Shterk, M. Karunakaran, I. D. Carja, D. Simic, I. Weilert, M. Klüppel, U. Giese, L. Cavallo, M. Rueping, M. Eddaoudi, J. Caro and J. Gascon, Solution processable metal-organic frameworks for mixed matrix membranes using porous liquids, *Nat. Mater.*, 2020, **19**, 1346–1353.
  - 35 M. S. Denny and S. M. Cohen, In Situ Modification of Metal-Organic Frameworks in Mixed-Matrix Membranes, *Angew. Chem., Int. Ed.*, 2015, **54**, 9029–9032.
  - 36 X. Li, Y. Zhang, Q. Xin, X. Ding, L. Zhao, H. Ye, L. Lin, H. Li and Y. Zhang, NH<sub>2</sub>-MIL-125 filled mixed matrix membrane contactor with SO<sub>2</sub> enrichment for flue gas desulfurization, *Chem. Eng. J.*, 2022, **428**, 132595.
  - 37 S. Friebe, A. Mundstock, D. Unruh, F. Renz and J. Caro, NH<sub>2</sub>-MIL-125 as membrane for carbon dioxide sequestration: Thin supported MOF layers contra Mixed-Matrix-Membranes, *J. Membr. Sci.*, 2016, **516**, 185–193.
  - 38 M. Waqas Anjum, B. Bueken, D. De Vos and I. F. J. Vankelecom, MIL-125(Ti) based mixed matrix membranes for CO<sub>2</sub> separation from CH<sub>4</sub> and N<sub>2</sub>, *J. Membr. Sci.*, 2016, **502**, 21–28.
  - 39 A. Morozan and F. Jaouen, Metal organic frameworks for electrochemical applications, *Energy Environ. Sci.*, 2012, **5**, 9269.
  - 40 H. Zhong, K. H. Ly, M. Wang, Y. Krupskaya, X. Han, J. Zhang, J. Zhang, V. Kataev, B. Buechner, I. M. Weidinger, S. Kaskel, P. Liu, M. Chen, R. Dong and X. Feng, A Phthalocyanine-Based Layered Two-Dimensional Conjugated Metal-Organic Framework as a Highly Efficient Electrocatalyst for the Oxygen Reduction Reaction, *Angew. Chem., Int. Ed.*, 2019, **58**, 10677–10682.
  - 41 J. Yang, H. Ye, F. Zhao and B. Zeng, A Novel Cu<sub>x</sub>O Nanoparticles@ZIF-8 Composite Derived from Core-Shell Metal-Organic Frameworks for Highly Selective Electrochemical Sensing of Hydrogen Peroxide, *ACS Appl. Mater. Interfaces*, 2016, **8**, 20407–20414.



- 42 B. Y. Xia, Y. Yan, N. Li, H. B. Wu, X. W. Lou and X. Wang, A metal-organic framework-derived bifunctional oxygen electrocatalyst, *Nat. Energy*, 2016, **1**, 15006.
- 43 C. R. Marshall, J. P. Dvorak, L. P. Twilight, L. Chen, K. Kadota, A. B. Andreeva, A. E. Overland, T. Ericson, A. F. Cozzolino and C. K. Brozek, Size-Dependent Properties of Solution-Processable Conductive MOF Nanocrystals, *J. Am. Chem. Soc.*, 2022, **144**, 5784–5794.
- 44 C. K. Brozek, D. Zhou, H. Liu, X. Li, K. R. Kittilstved and D. R. Gamelin, Soluble Supercapacitors: Large and Reversible Charge Storage in Colloidal Iron-Doped ZnO Nanocrystals, *Nano Lett.*, 2018, **18**, 3297–3302.
- 45 J. L. Mancuso, K. Fabrizio, C. K. Brozek and C. H. Hendon, On the limit of proton-coupled electronic doping in a Ti(IV)-containing MOF, *Chem. Sci.*, 2021, **12**, 11779–11785.
- 46 A. M. Schimpf, C. E. Gunthardt, J. D. Rinehart, J. M. Mayer and D. R. Gamelin, Controlling Carrier Densities in Photochemically Reduced Colloidal ZnO Nanocrystals: Size Dependence and Role of the Hole Quencher, *J. Am. Chem. Soc.*, 2013, **135**, 16569–16577.
- 47 A. M. Schimpf, S. D. Lounis, E. L. Runnerstrom, D. J. Milliron and D. R. Gamelin, Redox Chemistries and Plasmon Energies of Photodoped In<sub>2</sub>O<sub>3</sub> and Sn-Doped In<sub>2</sub>O<sub>3</sub> (ITO) Nanocrystals, *J. Am. Chem. Soc.*, 2015, **137**, 518–524.
- 48 L. De Trizio, R. Buonsanti, A. M. Schimpf, A. Llordes, D. R. Gamelin, R. Simonutti and D. J. Milliron, Nb-Doped Colloidal TiO<sub>2</sub> Nanocrystals with Tunable Infrared Absorption, *Chem. Mater.*, 2013, **25**, 3383–3390.
- 49 J. J. Araujo, C. K. Brozek, D. M. Kroupa and D. R. Gamelin, Degenerately n-Doped Colloidal PbSe Quantum Dots: Band Assignments and Electrostatic Effects, *Nano Lett.*, 2018, **18**, 3893–3900.
- 50 J. J. Araujo, C. K. Brozek, H. Liu, A. Merkulova, X. Li and D. R. Gamelin, Tunable Band-Edge Potentials and Charge Storage in Colloidal Tin-Doped Indium Oxide (ITO) Nanocrystals, *ACS Nano*, 2021, **15**, 14116–14124.
- 51 K. Fabrizio, K. N. Le, A. B. Andreeva, C. H. Hendon and C. K. Brozek, Determining Optical Band Gaps of MOFs, *ACS Mater. Lett.*, 2022, **4**, 457–463.
- 52 R. Ameis, S. Kremer and D. Reinen, Jahn-Teller effect of titanium(3+) in octahedral coordination: a spectroscopic study of hexachlorotitanate (TiCl<sub>6</sub><sup>3−</sup>) complexes, *Inorg. Chem.*, 1985, **24**, 2751–2754.
- 53 C. J. Ballhausen, *Introduction to Ligand Field Theory*, McGraw Hill Publishing Co., New York, 1962.
- 54 D. C. Harris and M. D. Bertolucci, *Symmetry and spectroscopy: an introduction to vibrational and electronic spectroscopy*, Dover Publications, New York, 1989.
- 55 T. Krämer, F. Tuna and S. D. Pike, Photo-redox reactivity of titanium-oxo clusters: mechanistic insight into a two-electron intramolecular process, and structural characterisation of mixed-valent Ti(III)/Ti(IV) products, *Chem. Sci.*, 2019, **10**, 6886–6898.
- 56 T. Hughbanks and R. Hoffmann, Molybdenum Chalcogenides: Clusters, Chains, and Extended Solids. The Approach to Bonding in Three Dimensions, *J. Am. Chem. Soc.*, 1983, **105**, 1150–1162.
- 57 G. Diao, L. Li and Z. Zhang, The electrochemical reduction of fullerenes, C<sub>60</sub> and C<sub>70</sub>, *Talanta*, 1996, **43**, 1633–1637.
- 58 Q. Zhao, T. D. Harris and T. A. Betley, [(<sup>H</sup>L)<sub>2</sub>Fe<sub>6</sub>(NCMe)<sub>m</sub>]<sup>n+</sup> (*m* = 0, 2, 4, 6; *n* = −1, 0, 1, 2, 3, 4, 6): an electron-transfer series featuring octahedral Fe<sub>6</sub> clusters supported by a hexaamide ligand platform, *J. Am. Chem. Soc.*, 2011, **133**, 8293–8306.
- 59 G. J. Lewis, J. D. Roth, R. A. Montag, L. K. Safford, X. Gao, S. C. Chang, L. F. Dahl and M. J. Weaver, Electroactive metal clusters as models of electrode surfaces: vibrational spectroelectrochemistry of seven redox forms of [Pt<sub>24</sub>(CO)<sub>30</sub>]<sub>*n*</sub> (*n* = 0 to −6) and comparison with potential-dependent spectra of carbon monoxide chemisorbed on platinum, *J. Am. Chem. Soc.*, 1990, **112**, 2831–2832.
- 60 J. D. Roth, G. J. Lewis, L. K. Safford, X. Jiang, L. F. Dahl and M. J. Weaver, Exploration of the Ionizable Metal Cluster-Electrode Surface Analogy: Infrared Spectroelectrochemistry of [Pt<sub>24</sub>(CO)<sub>30</sub>]<sub>*n*</sub>, [Pt<sub>26</sub>(CO)<sub>32</sub>]<sub>*n*</sub>, and [Pt<sub>38</sub>(CO)<sub>44</sub>]<sub>*n*</sub> (*n* = 0 to −10) and Comparisons with Potential-Dependent Spectra of CO Adlayers on Platinum Surfaces, *J. Am. Chem. Soc.*, 1992, **114**, 6159–6169.
- 61 E. Cattabriga, I. Ciabatti, C. Femoni, T. Funaioli, M. C. Iapalucci and S. Zacchini, Syntheses, Structures, and Electrochemistry of the Defective ccp [Pt<sub>33</sub>(CO)<sub>38</sub>]<sup>2−</sup> and the bcc [Pt<sub>40</sub>(CO)<sub>40</sub>]<sup>6−</sup> Molecular Nanoclusters, *Inorg. Chem.*, 2016, **55**, 6068–6079.
- 62 S. W. Boettcher, S. Z. Oener, M. C. Lonergan, Y. Surendranath, S. Ardo, C. Brozek and P. A. Kempler, Potentially Confusing: Potentials in Electrochemistry, *ACS Energy Lett.*, 2021, **6**, 261–266.

